Probing field-driven electron dynamics of gapped graphene by intensity-dependent valley polarization

Miao Yu,[1] Hongchuan Du,[2,*] Jia Tan,[3] Kunlong Liu,[4] Peixiang Lu,[1,5] and Yueming Zhou[1,†]

[1]*School of Physics and Wuhan National Laboratory for Optoelectronics, Huazhong University of Science and Technology, Wuhan 430074, China*

[2]*School of Nuclear Science and Technology, Lanzhou University, Lanzhou 730000, China*

[3]*Jiangsu Key Laboratory of Micro and Nano Heat Fluid Flow Technology and Energy Application, School of Physical Science and Technology, Suzhou University of Science and Technology, Suzhou, 215009, China*

[4]*School of Physical Sciences, Great Bay University, Dongguan 523000, China, and Great Bay Institute for Advanced Study, Dongguan 523000, China*

[5]*Optics Valley Laboratory, Wuhan 430074, China*

(Received 12 November 2023; revised 8 May 2024; accepted 20 May 2024; published 7 June 2024)

We investigate theoretically the laser intensity dependent valley polarization in gapped graphene driven by the circularly polarized pulse. The results show that the valley polarization without considering decoherence displays a nonmonotonic behavior as a function of the laser intensity. By analyzing the conduction-band electron distribution, we demonstrate that the decrease of the valley polarization in low laser intensity is caused by the change of dominant physical mechanisms, i.e., from few-photon to diabatic tunneling transitions. While in high laser intensity, the analysis of electron dynamics trajectories indicates that the intercycle interference determines the different k-resolved electron distributions in K and K′ valleys, influences the valley polarization, finally leads to the formation of a peak. Moreover, when the decoherence is considered, although the interference structure of the k-resolved electron distribution becomes blurred, the oscillation of valley polarization with the laser intensity is still present. Our work illustrates that the laser intensity can significantly influence the field-driven electron dynamics processes and can be as a knob to adjust the valley polarization in gapped graphene.

DOI: 10.1103/PhysRevA.109.063106

I. INTRODUCTION

The interaction between intense lasers and solids is a research hotspot in the fields of strong-field physics and condensed-matter physics. It has a potential for probing and controlling ultrafast carrier dynamics and material properties. Among them, the light-induced phenomena including high-harmonic generation [1–12] and field-driven current [13–15] provide routes for exploring electron-photon coupling [16,17], electron-density information [18], energy-band structure [19–21], Berry curvature [22] and more. So far, the underlying electronic dynamics have been extensively studied and two main mechanisms were proposed to understand these processes: interband polarization and intraband current [23–25]. However, deeper understanding of the underlying physics is still limited by the complicated structure and dynamical processes in solids. Because it is the fundamental of developing modern technologies, e.g., lightwave electronics [26] and information processing [27–29], comprehensive knowledge and control carrier dynamics are important in condensed-matter systems.

Two-dimensional materials with hexagonal lattice such as graphene and gapped graphene are a promising platform to study light-field-controlled carrier dynamics because of their ultrafast optical response, high carrier mobility, and high damage threshold [30,31]. In particular, compared with graphene, the gapped graphene has an extra electronic degree of freedom, i.e., the valley pseudospin. It is associated with the energy-degenerate valleys K and K′ in the lowest conduction band of the Brillouin zone. The flexible control over this valley degree of freedom has the potential in processing and storing quantum information [29,32,33], opening the applications of valleytronics [34–36]. Advances in the ultrafast laser technology have enabled the generation of precise subcycle laser pulse, which provides new opportunities for valleytronics [37–40]. Specifically, due to the valley optical selection rules for interband transition [41,42], circularly polarized lasers have been employed to obtain valley-selectivity excitation in gapped two-dimensional (2D) materials [32,33,43–46]. Besides, similar significant success has been achieved by linearly polarized laser [47–49].

The laser parameters are important for realizing the ultrafast lightwave control of electron dynamics. In this work, the laser intensity dependent valley polarization is theoretically investigated in gapped graphene. The simulation results show that the valley polarization without considering decoherence displays a nonmonotonic behavior as a function of the laser intensity, and there are valley and peaks. By analyzing the conduction band electron distributions, we demonstrate that the dynamics process is dominated by the few-photon transition at low laser intensity. Further increasing the laser intensity, the diabatic tunneling prevails and determines the

*duhch@lzu.edu.cn

†zhouymhust@hust.edu.cn

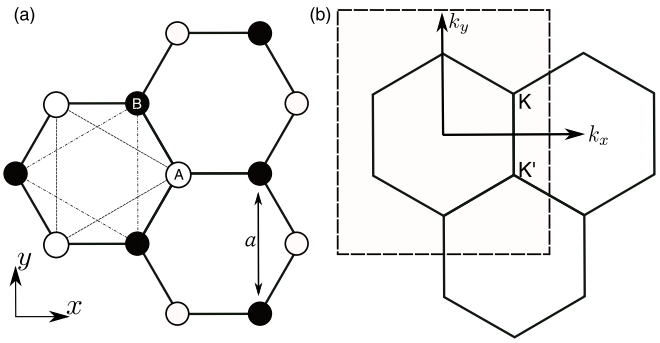

FIG. 1. (a) Hexagonal lattice structure of gapped graphene with two sublattices, A and B. (b) Corresponding Brillouin zone with two valleys K′ and K.

probability of electron being excited to the conduction band. Therefore, the decrease of valley polarization at low laser intensity is related to the change of dominant mechanism in interband transition. While at high laser intensity, i.e., the tunneling regime, the analysis of electron dynamics trajectories indicates that a peak is caused by the intercycle interference. Specifically, this interference determines the different k-resolved electron distributions in the K and K′ valleys, thus causing the oscillation of valley polarization with the laser intensity. Moreover, we show that this oscillation is still present when the decoherence is considered.

II. THEORETICAL METHODS

The unit cell of the gapped graphene arranged in a honeycomb lattice structure is illustrated in Fig. 1(a), which contains two sublattices labeled A and B. The corresponding Brillouin zone of the reciprocal lattice is shown in Fig. 1(b), in which the high-symmetry points [K $= (\frac{2\pi}{\sqrt{3}a}, \frac{2\pi}{3a})$ and K′ $= (\frac{2\pi}{\sqrt{3}a}, -\frac{2\pi}{3a})$ with the lattice constant $a = 0.246$ nm] are marked.

In the laser field, electron dynamics can be described by the time-dependent Schrödinger equation (TDSE). In the length gauge, the TDSE reads [atomic units (a.u.) are used throughout unless otherwise specified]

$$i\frac{\partial\Psi(t)}{\partial t} = [H_0 + \mathbf{r}\cdot\mathbf{F}(t)]\Psi(t), \tag{1}$$

where H_0 is the field-free Hamiltonian and $\mathbf{F}(t)$ is the electric field. In the nearest-neighbor tight-binding model, the reciprocal-space Hamiltonian $H_0(\mathbf{k})$ has the following form [50]:

$$H_0(\mathbf{k}) = \begin{bmatrix} \Delta/2 & \gamma f(\mathbf{k}) \\ \gamma f^*(\mathbf{k}) & -\Delta/2 \end{bmatrix}. \tag{2}$$

Here $\Delta = 2$ eV is the finite gap between the conduction band and valence band and $\gamma = -3.03$ eV is the hopping integral between nearest-neighbor atoms. The corresponding real system of gapped graphene can be obtained by doping and incommensurate substrate [51,52]. The function $f(\mathbf{k})$ describing the nearest-neighbor hopping is given by

$$f(\mathbf{k}) = \exp\left(i\frac{ak_x}{\sqrt{3}}\right) + 2\exp\left(-i\frac{ak_x}{2\sqrt{3}}\right)\cos\left(\frac{ak_y}{2}\right), \tag{3}$$

where $\mathbf{k} = (k_x, k_y)$ is the in-plane lattice momentum. Note that, although recent work has shown the defects of the nearest-neighbor tight-binding model in the study of solids harmonics [53], a previous study [54] and our calculations demonstrated that it is sufficient to use this model to reveal the ultrafast charge dynamics in graphene. By diagonalizing the Hamiltonian $H_0(\mathbf{k})$, the energies of conduction band and valence band can be determined as

$$E_c(\mathbf{k}) = +\sqrt{\gamma^2|f(\mathbf{k})|^2 + \frac{\Delta^2}{4}},$$
$$E_v(\mathbf{k}) = -\sqrt{\gamma^2|f(\mathbf{k})|^2 + \frac{\Delta^2}{4}}. \tag{4}$$

In gapped graphene, the applied ultrafast and strong laser field induces both the interband and intraband electron dynamics. According to the Bloch acceleration theorem [55], the temporal evolution of the electron wave packet in reciprocal space is $\mathbf{k}(t) = \mathbf{k}_0 - \int_{-\infty}^{t}\mathbf{E}(\tau)d\tau$, with initial momentum $\mathbf{k}_0$. The corresponding adiabatic wave functions, which are the solutions of Eq. (1) within a single band m without interband coupling, are well-known Houston functions [56],

$$\Phi^H_{m,\mathbf{k}(t)}(\mathbf{r},t) = \Psi^m_{\mathbf{k}(t)}(\mathbf{r})\exp\left[-i\phi^D_m(\mathbf{k}(t)) - i\phi^B_m(\mathbf{k}(t))\right], \tag{5}$$

where $m = c, v$ for conduction band and valence band, respectively. $\Psi^m_{\mathbf{k}(t)}(\mathbf{r})$ are the Bloch functions. $\phi^D_m(\mathbf{k}(t))$ and $\phi^B_m(\mathbf{k}(t))$ are the dynamics and Berry (geometry) phase [57,58] in the band m, respectively, and defined by

$$\phi^D_m(\mathbf{k}(t)) = \int_{-\infty}^{t} E_m[\mathbf{k}(\tau)]d\tau,$$
$$\phi^B_m(\mathbf{k}(t)) = \int_{-\infty}^{t}\mathbf{F}(\tau)\cdot\mathbf{d}_{mm}[\mathbf{k}(\tau)]d\tau. \tag{6}$$

Here, $\mathbf{d}_{mm}(\mathbf{k}) = i\langle\mu^m_{\mathbf{k}}(\mathbf{r})|\nabla_{\mathbf{k}}|\mu^m_{\mathbf{k}}(\mathbf{r})\rangle$ is the Berry connection with $\mu^m_{\mathbf{k}}$ the periodic part of Bloch function for the band m. The electron wave functions can be expanded using the Houston functions:

$$\Psi_{\mathbf{k}_0}(\mathbf{r},t) = \sum_{m=c,v} a_{m,\mathbf{k}_0}(t)\Phi^H_{m\mathbf{k}_0}(\mathbf{r},t). \tag{7}$$

By substituting this ansatz into TDSE, one can derive the two-level density-matrix equations (DMEs) [3,59], which are

$$\partial_t\Pi^{\mathbf{k}_0}(t) = -i\Omega_{cv}[\mathbf{k}(t)]\left[N^{\mathbf{k}_0}_v(t) - N^{\mathbf{k}_0}_c(t)\right]e^{i[\phi^D_{cv}(\mathbf{k}(t))+\phi^B_{cv}(\mathbf{k}(t))]} - \frac{\Pi^{\mathbf{k}_0}(t)}{T_2},$$
$$\partial_t N^{\mathbf{k}_0}_v(t) = -2\mathrm{Re}\{i\Omega^*_{cv}[\mathbf{k}(t)]\Pi^{\mathbf{k}_0}(t)e^{-i[\phi^D_{cv}(\mathbf{k}(t))+\phi^B_{cv}(\mathbf{k}(t))]}\},$$
$$\partial_t N^{\mathbf{k}_0}_c(t) = 2\mathrm{Re}\{i\Omega^*_{cv}[\mathbf{k}(t)]\Pi^{\mathbf{k}_0}(t)e^{-i[\phi^D_{cv}(\mathbf{k}(t))+\phi^B_{cv}(\mathbf{k}(t))]}\}, \tag{8}$$

where $\Pi^{\mathbf{k}_0}(t) = a_{c,\mathbf{k}_0}a^*_{v,\mathbf{k}_0}$ is the off-diagonal element of the density matrix, N_v and N_c are the populations of the valence band and conduction band, respectively. Initially, all electrons are in the valence band before the external field is turned on. $\Omega_{cv}[\mathbf{k}(t)] = \mathbf{F}(t)\cdot\mathbf{d}^{\mathbf{k}(t)}_{cv}$ is the Rabi frequency, and $\mathbf{d}_{cv}(\mathbf{k}) = i\langle\mu^c_{\mathbf{k}}(\mathbf{r})|\nabla_{\mathbf{k}}|\mu^v_{\mathbf{k}}(\mathbf{r})\rangle$ is the transition dipole moment. $\phi^D_{cv}(\mathbf{k}(t)) = \phi^D_c(\mathbf{k}(t)) - \phi^D_v(\mathbf{k}(t))$ and $\phi^B_{cv}(\mathbf{k}(t)) = \phi^B_c(\mathbf{k}(t)) - \phi^B_v(\mathbf{k}(t))$ are the transition dynamics phase (DP) and Berry phase (BP), respectively. Note that in

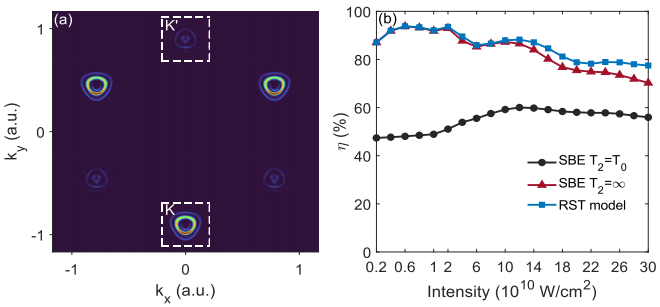

FIG. 2. (a) Conduction-band population of gapped graphene (band gap $\Delta = 2$ eV) after applying a right circularly polarized laser pulse with the frequency $\omega = 0.77$ eV and intensity $I_0 = 8\times10^{10}$ W/cm^2. The white squares show the areas around K′ and K points. (b) Valley polarization of gapped graphene as a function of the laser intensity. The black circles and red triangles illustrate the results obtained by solving the DMEs with dephasing times of $T_2 = T_0$ and $T_2 = \infty$. The prediction by the RST model is shown by the blue squares.

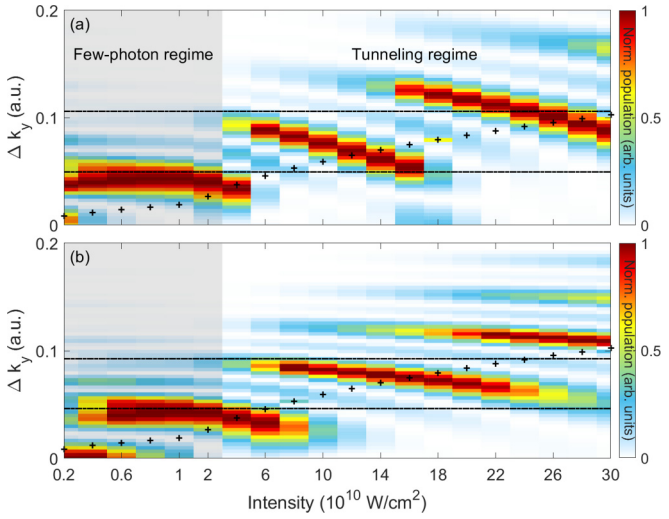

FIG. 3. Residual conduction-band populations (normalized to unity) as a function of the laser intensity and the distance from (a) K and (b) K′ points. Here, $\Delta k_y = k_{y0} - k_y$ and k_{y0} is the coordinate of K or K′ points on the k_y axis. The black dash-dotted curves represent the resonances, where the energy difference between the two bands corresponds to the photon energy $3\hbar\omega$ (lower lines) or $4\hbar\omega$ (higher lines). The black symbols indicate the maximum vector potential in the y direction.

Eq. (8), the decoherence is considered by phenomenologically adding the $-\Pi^{\mathbf{k}_0}(t)/T_2$ term, where T_2 is the dephasing time.

The response of the laser-driven electron in the gapped graphene can be obtained by solving the DMEs. In our simulation, the DMEs are numerically solved using the fourth-order Runge-Kutta method with a time step of $dt = 0.2$ a.u. The reciprocal space $k_x \in [-\frac{\sqrt{3}\pi}{a}, \frac{\sqrt{3}\pi}{a}]$ and $k_y \in [-\frac{2\pi}{a}, \frac{2\pi}{a}]$, shown as the dashed lines in Fig. 1(b), was sampled with a 761×817 grid. The convergence of the time step and space step in reciprocal space was tested.

III. RESULTS AND DISCUSSION

We apply an ultrafast right-circularly polarized pulse incident normally to the monolayer gapped graphene. The electric field is written as

$$\mathbf{F}(t) = F_0 f(t)[\cos(\omega t)\mathbf{e}_x + \sin(\omega t)\mathbf{e}_y], \tag{9}$$

where F_0 is the peak electric-field strength, $\omega = 0.77$ eV is the laser frequency, $\mathbf{e}_x$ and $\mathbf{e}_y$ are the unit vectors. $f(t)$ is the temporal envelope with a trapezoidal shape, raising linearly during one optical cycle (T_0), then keeping constant for two optical cycles and decreasing linearly during the last one optical cycle of the laser pulse.

A. Determination of the electron-excitation mechanism

Figure 2(a) illustrates the conduction-band population distribution over the whole Brillouin zone after excitation by the laser pulse with an intensity $I_0 = 8\times10^{10}$ W/cm^2, which is obtained by solving the DMEs with dephasing time $T_2 = \infty$. It is shown that the conduction-band population distribution in the K and K′ valleys is asymmetric, which agrees with the previous theoretical calculations [44,45]. To quantify this asymmetry, we define the valley polarization as

$$\eta = \frac{n_K - n_{K'}}{n_K + n_{K'}} \times 100\%,$$

where n_K ($n_{K'}$) is the electron occupation of valley K (K′), which is obtained by integrating the population around K (K′), as indicated by the white squares. The valley polarizations with respect to the laser intensity, which are simulated by the DMEs with $T_2 = \infty$ and $T_2 = T_0$, are shown in Fig. 2(b). We find that the valley polarization obtained with $T_2 = \infty$ clearly displays a nonmonotonic behavior as a function of the laser intensity, and there is a valley around 6×10^{10} W/cm^2 and a peak around 1.2×10^{11} W/cm^2.

To clarify the origin of this peculiar dependence, we further show the residual conduction-band populations as a function of the laser intensity and the distance from K and K′ points in Fig. 3. For comparison, the resonances, where the energy difference between the two bands ($E_g = E_c - E_v$) corresponds to the photon energy $3\hbar\omega$ or $4\hbar\omega$, are indicated by the black dash-dotted curves. By comparing the electron distribution and the position of resonance line, we found a change of interband excitation mechanism with increasing laser intensity. Specifically, in the weak-field region of $I_0 < 2\times10^{10}$ W/cm^2, the electrons transition to conduction band by few-photon excitation and are distributed along the $3\hbar\omega$ resonance line. Note that the energy shift of the position of electron maximum population from $3\hbar\omega$ is caused by the light-induced energy-band shift. Because the electron transition rate is proportional to the laser intensity in the few-photon regime, the conduction-band electron population increases with the laser intensity. Increasing the laser intensity to $I_0 = 4\times10^{10}$ W/cm^2, more electrons are excited to higher energy around the $E_g = 4\hbar\omega$ resonance line. In addition, most of the excited electrons are distributed away from the resonance line $3\hbar\omega$. This conduction-band electron distribution suggests that the electron transition mechanism is dominated by diabatic tunneling rather than few-photon excitation at this

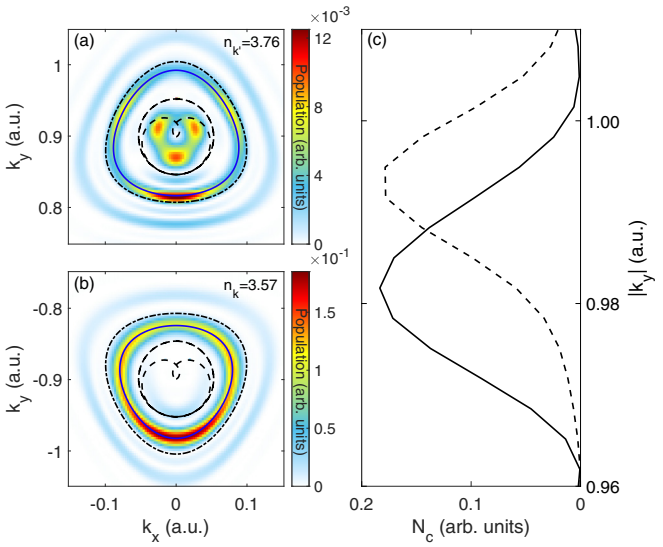

FIG. 4. Residual conduction-band populations around (a) K′ and (b) K points calculated by solving the DMEs ($T_2 = \infty$). The laser intensity is $I_0 = 8\times10^{10}$ W/cm^2. The black dash-dotted curves represent the resonances, where the energy difference between the two bands corresponds to the photon energy $4\hbar\omega$. The black dashed curves show the vector potential of laser pulse. The conduction-band maximum populations are illustrated by the blue solid curves, which are obtained by fitting with the function (a) $E_g = n_{K'}\hbar\omega$ and (b) $E_g = n_K\hbar\omega$. (c) The electron population on k_y axis extracted from panels (a) and (b). The black solid and dashed lines represent the electron distribution around the K and K′ points, respectively. For comparison, the electron population around the K′ point is scaled by a factor of 60.

intensity [45]. Therefore, the decrease of valley polarization at low laser intensity can be attributed to the change of dominant physical mechanism in interband transition.

B. Analysis of the *k*-resolved electron distribution

In the high laser intensity region of $I_0 = 4\times10^{10}$–1.6×10^{11} W/cm^2, most of the excited electrons are distributed between the resonance lines of $3\hbar\omega$ and $4\hbar\omega$, and the position of the conduction-band maximum population decreases with increasing laser intensity. Figures 4(a) and 4(b) further show the conduction-band electron distributions around K′ and K points induced by the laser field of $I_0 = 8\times10^{10}$ W/cm^2. By fitting the position of the maximum population in the conduction band with the function $E_g = n_{K'}\hbar\omega$ [Fig. 4(a)] or $E_g = n_K\hbar\omega$ [Fig. 4(b)], we find $n_{K'} = 3.76$ and $n_K = 3.57$, which are nonintegers, similar to the results in a recent study [60]. The difference of *k*-resolved electron distribution around the K and K′ points is further illustrated in Fig. 4(c). To better understand the physical processes, we resort to the reciprocal-space trajectory (RST) model [59]. Specifically, by substituting Eq. (7) into the TDSE, one can obtain the following differential equation:

$$\frac{d}{dt}a_{c,\mathbf{k}_0}(t) = -ia_{v,\mathbf{k}_0}(t)\Omega_{cv}[\mathbf{k}(t)]e^{i[\phi^D_{cv}(\mathbf{k}(t))+\phi^B_{cv}(\mathbf{k}(t))]}. \quad (10)$$

When the excitation probabilities are small (i.e., $a_{v,\mathbf{k}_0} \approx 1$) [3,59], the approximate solution of Eq. (10) is

$$a_{c,\mathbf{k}_0}(t) = -i\int_{-\infty}^{t}\Omega_{cv}[\mathbf{k}(\tau)]e^{i[\phi^D_{cv}(\mathbf{k}(\tau))+\phi^B_{cv}(\mathbf{k}(\tau))]}d\tau$$
$$= -i\int_{-\infty}^{t}|\Omega_{cv}[\mathbf{k}(\tau)]|e^{i\phi^{\rm tot}_{cv}(\mathbf{k}(\tau))}d\tau. \quad (11)$$

Here, $\phi^{\rm tot}_{cv}(\mathbf{k}(t)) = \phi^D_{cv}(\mathbf{k}(t)) + \phi^B_{cv}(\mathbf{k}(t)) + \phi^T_{cv}(\mathbf{k}(t))$ and $\phi^T_{cv}(\mathbf{k}(t)) = \arg\{\Omega_{cv}[\mathbf{k}(t)]\}$ are defined as the total phase and transition dipole moment phase (TDP), respectively. The results of the RST model are displayed by the blue squares in Fig. 2(b). It is shown that at low laser intensity, the value of valley polarization is consistent with that obtained by solving the DMEs with $T_2 = \infty$. While at higher laser intensity, the deviation of this result from the DMEs is caused by the low excitation probability approximation.

Figure 5 illustrates the conduction-band populations calculated by the RST model after excitation with the same laser parameters as Figs. 4(a) and 4(b), but discarding the Berry phase or transition dipole moment phase manually. In Figs. 5(a) and 5(b), the simulation results including the BP and TDP agree well with those from solving the DMEs with $T_2 = \infty$, i.e., Figs. 4(a) and 4(b), verifying the validity of the RST model in this laser parameter. The results of discarding the BP are shown in Figs. 5(c) and 5(d). It is shown that compared with the results in Figs. 5(a) and 5(b), the electron distributions around K′ point change significantly, but the electron distributions around the K point are almost invariant. When the TDP is discarded, compared with K′ point, the changes are more significant for the K point, as shown in Figs. 5(e) and 5(f). Furthermore, when both the BP and the TDP are discarded [Figs. 5(g) and 5(h)], the electron distributions is similar for the K′ and K points. These results unambiguously identify the effect of different kinds of phase on the *k*-resolved electron distribution. In the following, we explain the nonintegral $n_{K'}$ and n_K quantitatively by analyzing the reciprocal electron trajectories.

For the laser field with an intensity $I_0 = 8\times10^{10}$ W/cm^2, we choose initial momentum P1 = (0, −0.982), which is located at the maximum of conduction-band population around the K point and indicated by the black dot in Fig. 6(a). The corresponding field-driven dynamic trajectory is shown by the black dashed curve. Figure 6(b) illustrates the instantaneous transition rate $|\Omega_{cv}|$ and total phase $\phi^{\rm tot}_{cv}$ [Eq. (11)] with respect to the transition time. It is shown that for the initial momentum P1, the maximally instantaneous transition rate $|\Omega^{\rm max}_{cv}|$ is observed at time NT_0 (N = 1, 2, 3). Electrons excited at these times dominate the transition process. The interference between these electrons belongs to the intercycle interference, and its intensity is proportional to $\chi_{cv} = ||\Omega^{\rm max}_{cv}|(1 + e^{i\Delta\phi^{\rm tot}_{cv}})|$ [61]. Here, $\Delta\phi^{\rm tot}_{cv}$ is the difference of total phase between adjacent maximum transitions, as shown by the vertical dash-dotted blue lines in Fig. 6(b). Therefore, the electron transition probability is determined by the maximum transition rate $|\Omega^{\rm max}_{cv}|$ and the total phase difference $\Delta\phi^{\rm tot}_{cv}$. Figure 6(c) illustrates $|\Omega^{\rm max}_{cv}|$ and $\Delta\phi^{\rm tot}_{cv}$ for the electron with initial momentum along the k_y axis. The further calculated interference intensity χ_{cv} is shown by the black solid line in Fig. 6(d). For comparison, the conduction-band electron distribution on the k_y axis is extracted from Fig. 6(a) and

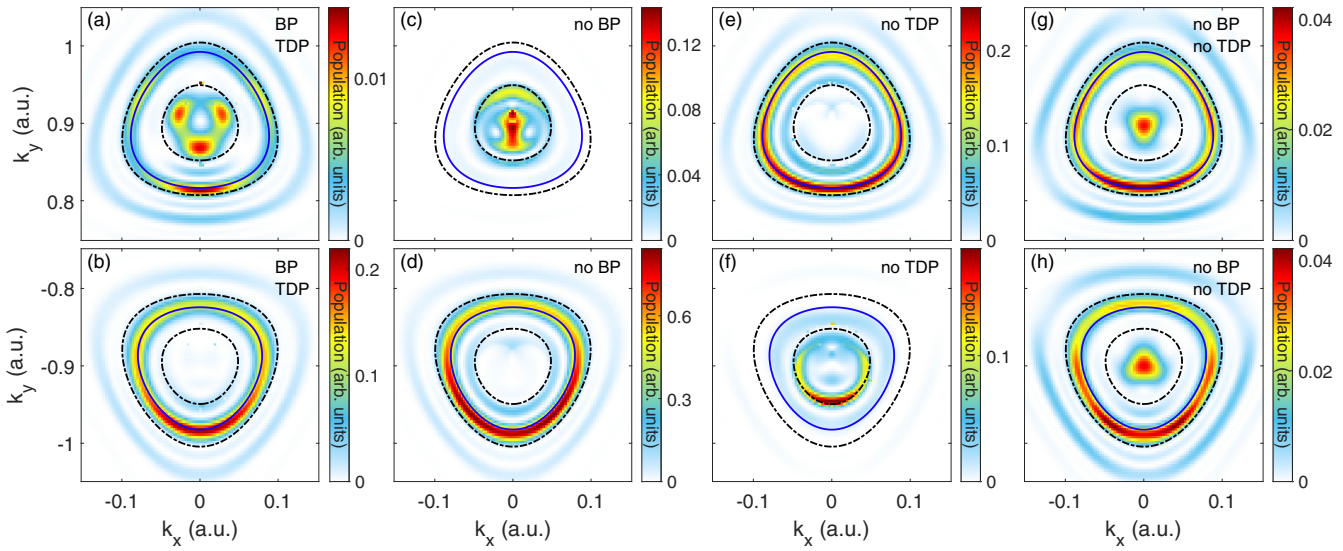

FIG. 5. (a), (c), (e), (g) Residual conduction-band populations around K′ and (b), (d), (f), (h) K points simulated by the RST model under the situations: (a), (b) Both the BP (Berry phase) and the TDP (transition dipole moment phase) are included. (c), (d) Only BP is discarded. (e), (f) Only TDP is discarded. (g), (h) Both the BP and TDP are discarded. The laser intensity is $I_0 = 8\times10^{10}$ W/cm^2. For comparison, the position of the conduction-band maximum populations calculated by solving the DMEs ($T_2 = \infty$) with same laser parameters, i.e., Figs. 4(a) and 4(b), are indicated by the blue solid curves. The black dash-dotted curves represent the resonances, where the energy difference between the two bands corresponds to the photon energy $3\hbar\omega$ or $4\hbar\omega$.

indicated by the blue dashed line in Fig. 6(d). The similarity between the distribution of interference intensity and lineout confirms that the k-resolved electron distribution is determined by the intercycle interference. For the initial momentum P1, although the maximum transition rate is smaller than that of some points, more electrons are eventually excited to the conduction band because $\Delta\phi_{cv}^{\rm tot}(\mathrm{P1}) = 5.87\pi$ is closer to $2N\pi$.

These results unambiguously indicate that in the diabatic tunneling regime, the intercycle interference determines the distribution of conduction-band populations at the non-integral photon energy. Besides, because the total phase difference $\Delta\phi_{cv}^{\rm tot}$ is related to the laser intensity, the position of conduction-band maximum population changes with increasing intensity.

Next, we investigate the difference of the position of conduction-band maximum populations between the K′ and K points, as shown in Figs. 4(a)–4(c). Compared with the K point, electrons around the K′ point are distributed at higher $|k_y|$, which corresponds to the higher energy in conduction band. To understand this difference, we choose two initial momenta $\mathrm{P2} = (0, 0.816)$ and $\mathrm{P3} = (0, -0.816)$. As indicated by the black dots in the insets of Figs. 7(a) and 7(c), P2 is located on the fitting curve of conduction-band maximum population around the K′ point ($n_{K'}\hbar\omega$), while P3 is away from the fitting curve of $n_K\hbar\omega$. Figures 7(a) and 7(c) illustrate the instantaneous transition rates and the total phases of P2 and P3. It is shown that the maximum instantaneous transition rate of two initial momenta is the same, but their total phase difference is different. For P2, the total phase difference is 9.88π, which is close to $2N\pi$. It is consistent with the *ab initio* result that P2 is located on the fitting curve of $n_{K'}\hbar\omega$. While for P3, the total phase difference is 6.17π. To determine the origin of this phase difference between $\Delta\phi_{cv}^{\rm tot}(\mathrm{P2})$ and $\Delta\phi_{cv}^{\rm tot}(\mathrm{p3})$, we further decompose the total phase difference into $\Delta\phi_{cv}^{\rm tot} = \Delta\phi_{cv}^{D} + \Delta\phi_{cv}^{T} + \Delta\phi_{cv}^{B}$, where $\Delta\phi_{cv}^{D}$, $\Delta\phi_{cv}^{T}$, and $\Delta\phi_{cv}^{B}$ are the difference of dynamics phase, transition dipole moment phase, and Berry phase between adjacent maximum transitions, respectively. Since the band structure of gapped graphene is symmetric about the k_x axis, $\Delta\phi_{cv}^{D}$ of P2 and P3 should be the same. Furthermore, for intercycle interference, $\Delta\phi_{cv}^{T}$ is zero or $2N\pi$ for P2 and P3. Therefore, the difference of the Berry phase difference of two points is determined as

$$\begin{aligned}\Delta\phi_{cv}^{B}(\mathrm{P2}) - \Delta\phi_{cv}^{B}(\mathrm{P3}) &= \left[\Delta\phi_{cv}^{\rm tot}(\mathrm{P2}) - \Delta\phi_{cv}^{\rm tot}(\mathrm{P3})\right] \\ &\quad - \left[\Delta\phi_{cv}^{T}(\mathrm{P2}) - \Delta\phi_{cv}^{T}(\mathrm{P3})\right] \\ &= 9.88\pi - 6.17\pi - 4\pi \\ &= -0.29\pi. \end{aligned} \tag{12}$$

Figures 7(b) and 7(d) illustrate the Berry phases with respect to the transition time of two initial momenta. It is shown that, for P2 and P3, the Berry phase difference is opposite. The difference of the Berry phase difference is -0.28π, which equals the result of Eq. (12). It indicates that the difference of total phase difference between P2 and P3 originates from the Berry phase. This opposite $\Delta\phi_{cv}^{B}$ influences the intercycle interference, resulting in a difference in the position of conduction-band maximum population between K′ and K points.

C. Scheme for increasing the valley polarization

We have quantitatively demonstrated that the position of conduction-band maximum population is determined by $|\Omega_{cv}^{\rm max}|$ and $\Delta\phi_{cv}^{\rm tot}$, which are related to the laser parameters. Therefore, by adjusting the laser parameters, more electrons will be excited to the conduction band when the

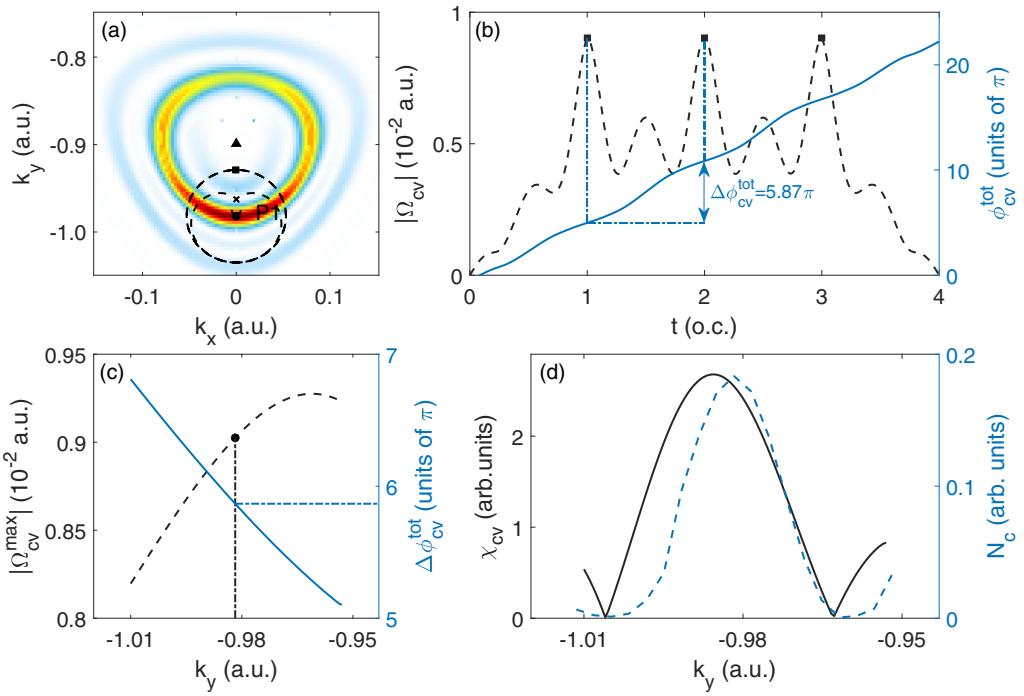

FIG. 6. (a), (b) Analysis of transition, dynamic trajectory and interference for initial momentum P1 = (0, −0.982) in the reciprocal space. (a) The black dot represents the initial momentum P1. For comparison, the K point is indicated by the black triangle. (b) The transition rate $|\Omega_{cv}|$ (black dashed line) and total phase $\phi_{cv}^{\rm tot}$ (blue solid line) with respect to the transition time for point P1. The maximum transition rates are marked with black squares. Meanwhile, the electron trajectory of point P1 is illustrated in black dashed curve of panel (a), and the position corresponding to the maximum transition rate is also represented by the black square. (c) The maximum transition rate $|\Omega_{cv}^{\rm max}|$ (black dashed line) and the total phase difference $\Delta\phi_{cv}^{\rm tot}$ (blue solid line) for initial momentum of electron along the k_y axis. (d) The intensity of intercycle interference χ_{cv} is illustrated by the black solid line. For comparison, the lineout taken along the k_y axis from panel (a) is shown by the blue dashed line.

electron with initial momentum $\rm P_K$ has maximal $|\Omega_{cv}^{\rm max}(\rm P_K)|$ and $\Delta\phi_{cv}^{\rm tot}(\rm P_K) = 2N\pi$. Moreover, due to the opposite Berry phase, the conduction-band populations around the K′ and K points could not be maximized simultaneously. This opens the opportunity to modulate the valley polarization. Figures 8(a) and 8(b) illustrate the conduction-band populations after excited by the laser pulse with an intensity $I_0 = 1.2\times10^{11}$ W/cm^2. In particular, the position of conduction-band maximum population around the K point, as shown in Fig. 8(b), almost coincides with the vector potential of laser pulse. Figures 8(c) and 8(d) illustrate the corresponding $|\Omega_{cv}^{\rm max}|$ and $\Delta\phi_{cv}^{\rm tot}$ as a function of the initial momentum of electron around the K′ and K points, respectively. It is shown that at the initial momentum $\rm P_K = (0, -0.973)$, as indicated by the black dot in Fig. 8(d), $|\Omega_{cv}^{\rm max}(\rm P_K)|$ maximizes and $\Delta\phi_{cv}^{\rm tot}(\rm P_K) = 5.99\pi$. For the initial momentum $\rm P_{K'} = (0, 0.973)$, $|\Omega_{cv}^{\rm max}(\rm P_{K'})|$ maximizes while $\Delta\phi_{cv}^{\rm tot}(\rm P_{K'}) = 9.47\pi$. In this case, only the population of the excited electron around K point is increased by intercycle interference, resulting that the difference between n_K and $n_{K'}$ and thus the valley polarization enhance. These results are consistent with that of Fig. 2(b), where the valley polarization peaks at laser intensity of $I_0 = 1.2\times10^{11}$ W/cm^2. With the increase of laser intensity, the positions of conduction-band maximum populations of the K′ and K points change, which further weakens the valley polarization. These results indicate that in the gapped graphene, the valley polarization can be modulated by changing the laser intensity and does not monotonically increase as the laser intensity increases.

D. The effect of decoherence

It is well known that decoherence is an important physical process in solids. Previous studies have shown the effect of decoherence by phenomenologically incorporating a constant dephasing time T_2 in calculation. Note that due to the complexity of the decoherence mechanism, the value of the dephasing time has not been determined, and different values have been used in previous studies [3,62–64]. In our work, we fix $T_2 = T_0$ as the effective interband dephasing time to investigate the effect of decoherence on the k-resolved electron distribution and valley polarization. The black circles in Fig. 2(b) illustrate the valley polarization for a dephasing time of $T_2 = T_0$, which shows a clear oscillation with laser intensity. In addition, the valley polarization simulated with $T_2 = T_0$ peaks at the laser intensity of $I_0 = 1.2\times10^{11}$ W/cm^2, which is consistent with the result simulated with $T_2 = \infty$. While the difference between the two results can be attributed to the deexcitation of conduction-band electron induced by the decoherence, which is stronger for the distribution of conduction band with fewer excited electrons. Therefore, at lower laser intensity, the conduction-band electron population and thus the valley polarization obtained with $T_2 = T_0$ is different for the results of $T_2 = \infty$. This difference makes it possible

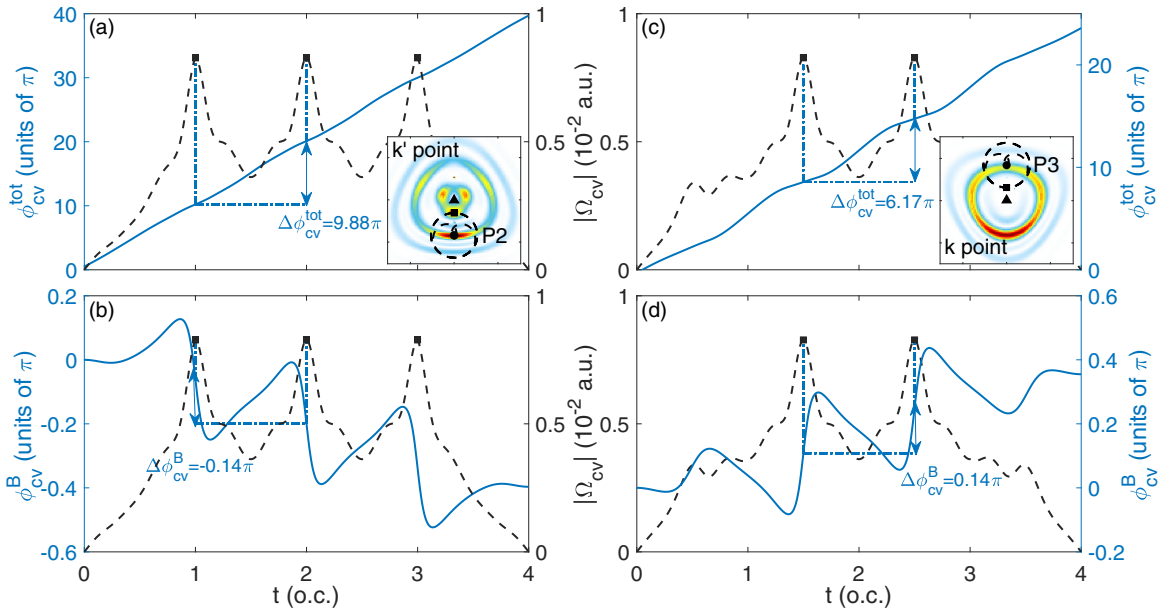

FIG. 7. The total phase $\phi_{cv}^{\rm tot}$ and Berry phase ϕ_{cv}^{B} for the initial point P2 = (0, 0.816) around K′ is shown by blue solid line in panels (a) and (b), respectively. For comparison, the transition rate is shown by the black dashed line. The inset at the bottom right corner of panel (a) illustrates the corresponding electron trajectory. (c), (d) Same as panels (a), (b), but for the initial point P3 = (0, −0.816) around K.

to determine the dephasing time in terms of the influence of decoherence on the valley polarization in the future.

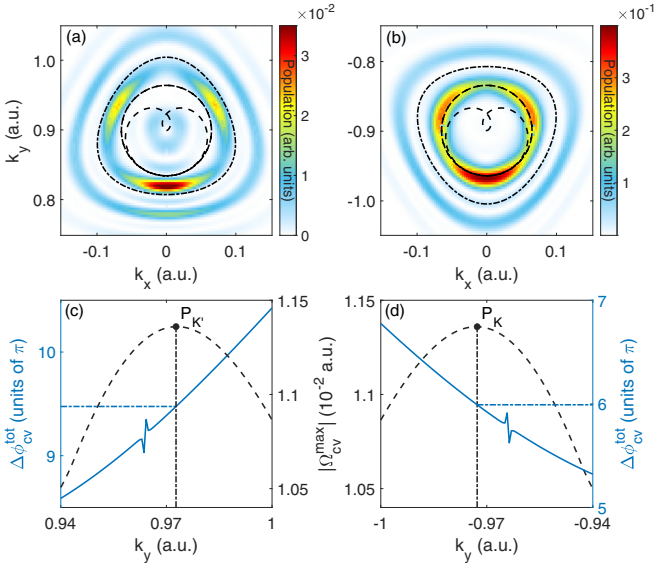

FIG. 8. (a), (b) Residual conduction-band populations around (a) K′ and (b) K points calculated by solving the DMEs ($T_2 = \infty$). The laser intensity is $I_0 = 1.2\times10^{11}$ W/cm^2. The black dash-dotted curves represent the resonances, where the energy difference between the two bands corresponds to the photon energy $4\hbar\omega$. The black dashed curves show the vector potential of laser pulse. (c), (d) The maximum transition rates $|\Omega_{cv}^{\rm max}|$ (black dashed lines) and the total phase differences $\Delta\phi_{cv}^{\rm tot}$ (blue solid lines) with respect to the initial momentum of electron along the k_y axis. The black dots represent the initial momenta $\mathrm{P}_{K'} = (0, 0.973)$, $\mathrm{P}_{K} = (0, -0.973)$ where $|\Omega_{cv}^{\rm max}|$ maximizes. (c) $\Delta\phi_{cv}^{\rm tot}(\mathrm{P}_{K'})$ and (d) $\Delta\phi_{cv}^{\rm tot}(\mathrm{P}_{K})$ are marked by the blue dash-dotted lines.

In Fig. 9, we further illustrate the conduction-band populations calculated by solving the DMEs with $T_2 = T_0$ after excitation with the laser intensity of $I_0 = 8\times10^{10}$ W/cm^2 [Figs. 9(a) and 9(b)] and $I_0 = 1.2\times10^{11}$ W/cm^2 [Figs. 9(c)

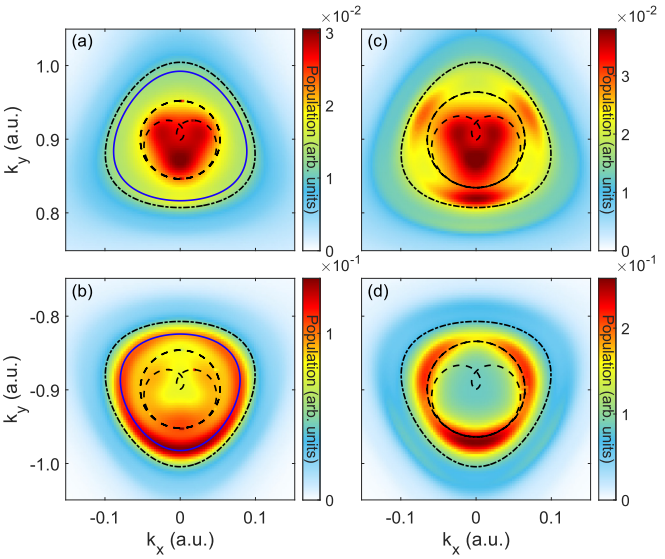

FIG. 9. Conduction-band populations after excitation around (a), (c) K′ and (b), (d) K points calculated by solving the DMEs ($T_2 = T_0$). The laser intensities are (a), (b) $I_0 = 8\times10^{10}$ W/cm^2 and (c), (d) $I_0 = 1.2\times10^{11}$ W/cm^2. The black dash-dotted curves represent the resonances, where the energy difference between the two bands corresponds to the photon energy $4\hbar\omega$. The black dashed curves show the vector potential of laser pulse. For comparison, the positions of conduction-band maximum population calculated by solving the DMEs ($T_2 = \infty$) with $I_0 = 8\times10^{10}$ W/cm^2 are shown by the blue solid curves in panels (a), (b).

and 9(d)]. It is shown that, except for Fig. 9(a), the k-resolved electron distributions obtained by solving the DMEs with $T_2 = T_0$ are similar to that obtained with $T_2 = \infty$. Specifically, at the laser intensity of $I_0 = 8\times10^{10}$ W/cm^2, for the K point, the position of the conduction-band maximum population obtained with $T_2 = T_0$ is the same as that obtained with $T_2 = \infty$, as shown by the blue solid curve in Fig. 9(b). Furthermore, in the laser intensity of $I_0 = 1.2\times10^{11}$ W/cm^2, the position of the conduction-band maximum population of the K point almost coincides with the vector potential of laser pulse, which is consistent with the result shown in Fig. 8(b). Therefore, the valley polarization can be modulated through changing the laser intensity. Even if decoherence impacts the k-resolved electron distribution and thus the value of valley polarization. The oscillation of valley polarization with laser intensity presents.

IV. CONCLUSION

We investigate theoretically the valley polarization in gapped graphene driven by a right-circularly polarized pulse and analyze the k-resolved electron distributions in the conduction band. The valley polarization obtained by solving the DMEs with the dephasing time $T_2 = \infty$ reveals a nonmonotonic dependence on the laser intensity, and there are valley and peaks. By analyzing the conduction-band populations, we find that different physical mechanisms dominate the interband transition at different laser intensities. In the low-intensity limit, few-photon transition prevails, with the increase of laser intensity the dominant mechanism is diabatic tunneling. The transition of excitation mechanism results in the decrease of valley polarization at low laser intensity.

Further increasing the laser intensity, we find that the excited electrons in the conduction band are distributed at the energy $E_g = n_{\mathrm{K}'}\hbar\omega$ and $E_g = n_{\mathrm{K}}\hbar\omega$, where $n_{\mathrm{K}'}$ and n_{K} are nonintegers. By analyzing the electron dynamics trajectories, we demonstrate that the k-resolved electron distribution is determined by the intercycle interference. The position of the electron maximum populations around the K and K$'$ points can be quantitatively identified by the instantaneous transition rate $|\Omega_{cv}^{\max}|$ and the total phase difference $\Delta\phi_{cv}^{\mathrm{tot}}$ between adjacent maximum transitions, which are related to the laser parameters. Therefore, by adjusting the laser intensity, the k-resolved electron transition probability can be modulated, which further influences the valley polarization. These results clarify the origin of the last peak of valley polarization in the diabatic tunneling regime.

Besides, the effect of decoherence has been considered by phenomenologically introducing the dephasing time. The results indicate that even if decoherence influences the k-resolved electron distribution, the oscillation of valley polarization with laser intensity presents. In summary, by clarifying the dependence of valley polarization on laser intensity, we provide an intuitive physical picture for field-driven electron dynamics of gapped graphene. Furthermore, we propose a scheme for modulating the valley polarization, which is one of the manifestations of optical control over the light-mater interaction process. Our study is useful for the fundamental understanding and further applications of strong-field-driven electrons in two-dimensional materials, including graphene and transition-metal dichalcogenide monolayers.

ACKNOWLEDGMENTS

This work is supported by National Key Research and Development Program of China (Grant No. 2019YFA0308300), the National Natural Science Foundation of China (Grants No. 12374264, No. 12274188, No. 12174133, and No. 12204341), the Fundamental Research Funds for the Central Universities (Grant No. lzujbky-2023-ey08), and the Natural Science Foundation of Jiangsu Province (Grant No. BK20220633). The computation was completed using the HPC Platform of Huazhong University of Science and Technology.

[1] S. Ghimire, A. D. DiChiara, E. Sistrunk, P. Agostini, L. F. DiMauro, and D. A. Reis, Observation of high-order harmonic generation in a bulk crystal, Nat. Phys. **7**, 138 (2011).

[2] O. Schubert, M. Hohenleutner, F. Langer, B. Urbanek, C. Lange, U. Huttner, D. Golde, T. Meier, M. Kira, S. W. Koch, and R. Huber, Sub-cycle control of terahertz high-harmonic generation by dynamical Bloch oscillations, Nat. Photon. **8**, 119 (2014).

[3] G. Vampa, C. R. McDonald, G. Orlando, D. D. Klug, P. B. Corkum, and T. Brabec, Theoretical analysis of high-harmonic generation in solids, Phys. Rev. Lett. **113**, 073901 (2014).

[4] N. Yoshikawa, T. Tamaya, and K. Tanaka, High-harmonic generation in graphene enhanced by elliptically polarized light excitation, Science **356**, 736 (2017).

[5] S. Jiang, J. Chen, H. Wei, C. Yu, R. Lu, and C. D. Lin, Role of the transition dipole amplitude and phase on the generation of odd and even high-order harmonics in crystals, Phys. Rev. Lett. **120**, 253201 (2018).

[6] J. Li, X. Zhang, S. Fu, Y. Feng, B. Hu, and H. Du, Phase invariance of the semiconductor Bloch equations, Phys. Rev. A **100**, 043404 (2019).

[7] M. S. Mrudul, N. Tancogne-Dejean, A. Rubio, and G. Dixit, High-harmonic generation from spin-polarised defects in solids, npj Comput. Mater. **6**, 10 (2020).

[8] L. Yue and M. B. Gaarde, Imperfect recollisions in high-harmonic generation in solids, Phys. Rev. Lett. **124**, 153204 (2020).

[9] M. S. Mrudul and G. Dixit, High-harmonic generation from monolayer and bilayer graphene, Phys. Rev. B **103**, 094308 (2021).

[10] Y. Kobayashi, C. Heide, H. K. Kelardeh, A. Johnson, F. Liu, T. F. Heinz, D. A. Reis, and S. Ghimire, Polarization flipping of even-order harmonics in monolayer transition-metal dichalcogenides, Ultrafast Sci. **2021**, 9820716 (2021).

[11] R. Zuo, A. Trautmann, G. Wang, W. Hannes, S. Yang, X. Song, T. Meier, M. Ciappina, H. T. Duc, and W. Yang, Neighboring

atom collisions in solid-state high harmonic generation, Ultrafast Sci. **2021**, 9861923 (2021).
[12] E. Goulielmakis and T. Brabec, High harmonic generation in condensed matter, Nat. Photon. **16**, 411 (2022).
[13] T. Higuchi, C. Heide, K. Ullmann, H. B. Weber, and P. Hommelhoff, Light-field-driven currents in graphene, Nature (London) **550**, 224 (2017).
[14] C. Heide, T. Higuchi, H. B. Weber, and P. Hommelhoff, Coherent electron trajectory control in graphene, Phys. Rev. Lett. **121**, 207401 (2018).
[15] O. Neufeld, N. Tancogne-Dejean, U. De Giovannini, H. Hübener, and A. Rubio, Light-driven extremely nonlinear bulk photogalvanic currents, Phys. Rev. Lett. **127**, 126601 (2021).
[16] M. R. Bionta, E. Haddad, A. Leblanc, V. Gruson, P. Lassonde, H. Ibrahim, J. Chaillou, N. Émond, M. R. Otto, Á. Jiménez-Galán, R. E. F. Silva, M. Ivanov, B. J. Siwick, M. Chaker, and F. Légaré, Tracking ultrafast solid-state dynamics using high harmonic spectroscopy, Phys. Rev. Res. **3**, 023250 (2021).
[17] O. Neufeld, J. Zhang, U. De Giovannini, H. Hübener, and A. Rubio, Probing phonon dynamics with multidimensional high harmonic carrier-envelope-phase spectroscopy, Proc. Natl. Acad. Sci. USA **119**, e2204219119 (2022).
[18] H. Lakhotia, H. Y. Kim, M. Zhan, S. Hu, S. Meng, and E. Goulielmakis, Laser picoscopy of valence electrons in solids, Nature (London) **583**, 55 (2020).
[19] G. Vampa, T. J. Hammond, N. Thiré, B. E. Schmidt, F. Légaré, C. R. McDonald, T. Brabec, D. D. Klug, and P. B. Corkum, All-optical reconstruction of crystal band structure, Phys. Rev. Lett. **115**, 193603 (2015).
[20] A. A. Lanin, E. A. Stepanov, A. B. Fedotov, and A. M. Zheltikov, Mapping the electron band structure by intraband high-harmonic generation in solids, Optica **4**, 516 (2017).
[21] L. Lü and X. Bian, Ultrafast intraband electron dynamics of preexcited SiO_2, Opt. Express **28**, 13432 (2020).
[22] T. T. Luu and H. J. Wörner, Measurement of the Berry curvature of solids using high-harmonic spectroscopy, Nat. Commun. **9**, 916 (2018).
[23] D. Golde, T. Meier, and S. W. Koch, High harmonics generated in semiconductor nanostructures by the coupled dynamics of optical inter- and intraband excitations, Phys. Rev. B **77**, 075330 (2008).
[24] T. T. Luu, M. Garg, S. Y. Kruchinin, A. Moulet, M. T. Hassan, and E. Goulielmakis, Extreme ultraviolet high-harmonic spectroscopy of solids, Nature (London) **521**, 498 (2015).
[25] G. Vampa, T. J. Hammond, N. Thiré, B. E. Schmidt, F. Légaré, C. R. McDonald, T. Brabec, and P. B. Corkum, Linking high harmonics from gases and solids, Nature (London) **522**, 462 (2015).
[26] F. Krausz and M. I. Stockman, Attosecond metrology: from electron capture to future signal processing, Nat. Photon. **8**, 205 (2014).
[27] T. D. Ladd, F. Jelezko, R. Laflamme, Y. Nakamura, C. Monroe, and J. L. O'Brien, Quantum computers, Nature (London) **464**, 45 (2010).
[28] G. Aivazian, Z. Gong, A. M. Jones, R. Chu, J. Yan, D. G. Mandrus, C. Zhang, D. Cobden, W. Yao, and X. Xu, Magnetic control of valley pseudospin in monolayer WSe_2, Nat. Phys. **11**, 148 (2015).
[29] G. Wang, X. Marie, B. L. Liu, T. Amand, C. Robert, F. Cadiz, P. Renucci, and B. Urbaszek, Control of exciton valley coherence in transition metal dichalcogenide monolayers, Phys. Rev. Lett. **117**, 187401 (2016).
[30] A. H. Castro Neto, F. Guinea, N. M. R. Peres, K. S. Novoselov, and A. K. Geim, The electronic properties of graphene, Rev. Mod. Phys. **81**, 109 (2009).
[31] F. J. García de Abajo, Graphene plasmonics: Challenges and opportunities, ACS Photon. **1**, 135 (2014).
[32] K. F. Mak, K. He, J. Shan, and T. F. Heinz, Control of valley polarization in monolayer MoS_2 by optical helicity, Nat. Nanotechnol. **7**, 494 (2012).
[33] H. Zeng, J. Dai, W. Yao, D. Xiao, and X. Cui, Valley polarization in MoS_2 monolayers by optical pumping, Nat. Nanotechnol. **7**, 490 (2012).
[34] O. Gunawan, Y. P. Shkolnikov, K. Vakili, T. Gokmen, E. P. De Poortere, and M. Shayegan, Valley susceptibility of an interacting two-dimensional electron system, Phys. Rev. Lett. **97**, 186404 (2006).
[35] A. Rycerz, J. Tworzydło, and C. W. J. Beenakker, Valley filter and valley valve in graphene, Nat. Phys. **3**, 172 (2007).
[36] S. A. Vitale, D. Nezich, J. O. Varghese, P. Kim, N. Gedik, P. Jarillo-Herrero, D. Xiao, and M. Rothschild, Valleytronics: Opportunities, challenges, and paths forward, Small **14**, 1801483 (2018).
[37] J. R. Schaibley, H. Yu, G. Clark, P. Rivera, J. S. Ross, K. L. Seyler, W. Yao, and X. Xu, Valleytronics in 2D materials, Nat. Rev. Mater. **1**, 16055 (2016).
[38] F. Langer, C. P. Schmid, S. Schlauderer, M. Gmitra, J. Fabian, P. Nagler, C. Schüller, T. Korn, P. G. Hawkins, J. T. Steiner, U. Huttner, S. W. Koch, M. Kira, and R. Huber, Lightwave valleytronics in a monolayer of tungsten diselenide, Nature (London) **557**, 76 (2018).
[39] M. S. Mrudul, Á. Jiménez-Galán, M. Ivanov, and G. Dixit, Light-induced valleytronics in pristine graphene, Optica **8**, 422 (2021).
[40] N. Rana and G. Dixit, All-optical ultrafast valley switching in two-dimensional materials, Phys. Rev. Appl. **19**, 034056 (2023).
[41] D. Xiao, W. Yao, and Q. Niu, Valley-contrasting physics in graphene: Magnetic moment and topological transport, Phys. Rev. Lett. **99**, 236809 (2007).
[42] W. Yao, D. Xiao, and Q. Niu, Valley-dependent optoelectronics from inversion symmetry breaking, Phys. Rev. B **77**, 235406 (2008).
[43] K. F. Mak, K. L. McGill, J. Park, and P. L. McEuen, The valley hall effect in MoS_2 transistors, Science **344**, 1489 (2014).
[44] S. A. Oliaei Motlagh, J.-S. Wu, V. Apalkov, and M. I. Stockman, Femtosecond valley polarization and topological resonances in transition metal dichalcogenides, Phys. Rev. B **98**, 081406(R) (2018).
[45] S. A. O. Motlagh, F. Nematollahi, V. Apalkov, and M. I. Stockman, Topological resonance and single-optical-cycle valley polarization in gapped graphene, Phys. Rev. B **100**, 115431 (2019).
[46] Á. Jiménez-Galán, R. E. F. Silva, O. Smirnova, and M. Ivanov, Lightwave control of topological properties in 2D materials for sub-cycle and non-resonant valley manipulation, Nat. Photon. **14**, 728 (2020).
[47] Á. Jiméenez-Galán, R. E. F. Silva, O. Smirnova, and M. Ivanov, Sub-cycle valleytronics: control of valley polarization using few-cycle linearly polarized pulses, Optica **8**, 277 (2021).

[48] H. K. Kelardeh, U. Saalmann, and J. M. Rost, Ultrashort laser-driven dynamics of massless dirac electrons generating valley polarization in graphene, Phys. Rev. Res. **4**, L022014 (2022).

[49] U. Saalmann and J. M. Rost, Local excitation and valley polarization in graphene with multi-harmonic pulses, Faraday Discuss. **237**, 368 (2022).

[50] T. G. Pedersen, A.-P. Jauho, and K. Pedersen, Optical response and excitons in gapped graphene, Phys. Rev. B **79**, 113406 (2009).

[51] M. S. Nevius, M. Conrad, F. Wang, A. Celis, M. N. Nair, A. Taleb-Ibrahimi, A. Tejeda, and E. H. Conrad, Semiconducting graphene from highly ordered substrate interactions, Phys. Rev. Lett. **115**, 136802 (2015).

[52] X. Xu, C. Liu, Z. Sun, T. Cao, Z. Zhang, E. Wang, Z. Liu, and K. Liu, Interfacial engineering in graphene bandgap, Chem. Soc. Rev. **47**, 3059 (2018).

[53] Y. Zhang, M. Zhang, W. Yang, H. Yu, M. S. Si, S. Xue, and H. Du, Defects of the nearest-neighbor tight-binding model in the study of solid harmonics, Phys. Rev. A **108**, 043508 (2023).

[54] Q. Z. Li, P. Elliott, J. K. Dewhurst, S. Sharma, and S. Shallcross, *Ab initio* study of ultrafast charge dynamics in graphene, Phys. Rev. B **103**, L081102 (2021).

[55] F. Bloch, Über die quantenmechanik der elektronen in kristallgittern, Eur. Phys. J. A **52**, 555 (1929).

[56] W. V. Houston, Acceleration of electrons in a crystal lattice, Phys. Rev. **57**, 184 (1940).

[57] M. V. Berry, Quantal phase factors accompanying adiabatic changes, Proc. R. Soc. London, Ser. A **392**, 45 (1984).

[58] D. Xiao, M.-C. Chang, and Q. Niu, Berry phase effects on electronic properties, Rev. Mod. Phys. **82**, 1959 (2010).

[59] L. Li, P. Lan, X. Zhu, T. Huang, Q. Zhang, M. Lein, and P. Lu, Reciprocal-space-trajectory perspective on high-harmonic generation in solids, Phys. Rev. Lett. **122**, 193901 (2019).

[60] A. Galler, A. Rubio, and O. Neufeld, Mapping light-dressed Floquet bands by highly nonlinear optical excitations and valley polarization, J. Phys. Chem. Lett. **14**, 11298 (2023).

[61] D. G. Arbó, K. L. Ishikawa, K. Schiessl, E. Persson, and J. Burgdörfer, Intracycle and intercycle interferences in above-threshold ionization: The time grating, Phys. Rev. A **81**, 021403(R) (2010).

[62] M. S. Wismer, S. Y. Kruchinin, M. Ciappina, M. I. Stockman, and V. S. Yakovlev, Strong-field resonant dynamics in semiconductors, Phys. Rev. Lett. **116**, 197401 (2016).

[63] C. Heide, T. Eckstein, T. Boolakee, C. Gerner, H. B. Weber, I. Franco, and P. Hommelhoff, Electronic coherence and coherent dephasing in the optical control of electrons in graphene, Nano Lett. **21**, 9403 (2021).

[64] Y. Wang, T. Shao, X. Li, Y. Liu, P. Jiang, W. Zheng, L. Zhang, X. Bian, Y. Liu, Q. Gong, and C. Wu, Trajectory-controlled high-order harmonic generation in ZnO crystals. Opt. Express **31**, 3379 (2023).